**International Journal of Minerals, Metallurgy and Materials**
**Accepted manuscript, https://doi.org/10.1007/s12613-024-3072-8**


# Optimization and mechanism analysis of multi-solid wastes-based geopolymer using response surface methodology

*Muyang Huang*[1,2)], *Shenxu Bao*[1,2,3),✉], *Yimin Zhang*[2,3)], *Mengke Li*[1,2)], *Chong Deng*[4)], *and Wenhan Chen*[4)]

1) Key Laboratory of Green Utilization of Critical Non-metallic Mineral Resources, Ministry of Education, Wuhan University of Technology, Wuhan 430070, China

2) School of Resources and Environmental Engineering, Wuhan University of Technology, Wuhan 430070, China

3) Hubei Collaborative Innovation Center for High Efficient Utilization of Vanadium Resources, Wuhan University of Science and Technology, Wuhan 430081, China

4) CCCC Luhang New Material Technology Guangxi Co., Ltd., Wuzhou 543002, China

✉Corresponding author: Shenxu Bao E-mail: sxbao@whut.edu.cn

**Abstract:** The escalating production of industrial solid waste, in conjunction with the dwindling availability of natural resources, has intensified focus on waste recycling. However, the heterogeneity and complexity of waste pose significant challenges to the determination of process parameters. In this study, burnt coal cinder (BCC), granite powder (GP), and high-calcium fly ash (Class-C FA) was as raw materials and the response surface methodology (RSM) and single-factor experiments were applied to optimize the process parameters for geopolymer preparation. The optimized precursor powder composition was determined to be a mass ratio of 1.6: 0.9: 7.3 for BCC, GP, and Class-C FA. The NaOH-precursor powder ratio and liquid-solid ratio

were adjusted to 0.084 and 0.222, respectively. The curing condition was set at 80°C for 24 h. The resulting 28-d aged multi-solid wastes-based geopolymer exhibited high compressive strength of 61.34 MPa. The microstructure, mineral phase, and atomic bonding of geopolymers were investigated using XRD, TA, FTIR, and SEM-EDS techniques. The findings indicate that the compressive strength of geopolymer is most significantly influenced by the Class-C FA, followed by BCC. Furthermore, minor addition of GP can optimize structural density of geopolymer. The Ca present in the Class-C FA participates in the geopolymerization, forming hybrid N-(C)-A-S-H gel. RSM optimization facilitates the synergistic utilization of multi-solid wastes, ensuring an even distribution of gel and filler. This research establishes a theoretical framework for optimizing the preparation parameters of multi-solid wastes-based geopolymer and its subsequent applications. It holds significant scientific implications for the circular economy, resource transformation, and environmental conservation.

**Keywords:** Multi-solid wastes; Geopolymer; Response surface methodology; Process parameters; Synergistic effect



## 1. Introduction

Facilitating technological advancements and material innovations geared towards efficient recycling and environmentally responsible disposal of solid waste is pivotal in tackling environmental pollution and alleviating resource scarcity [1-4]. As solid waste accumulates rapidly, research has increasingly focused on using it to produce building materials, with geopolymer standing out as a sustainable and eco-friendly option [5-7]. Typically, geopolymer is prepared from high-activity aluminosilicate

precursors such as metakaolin and low-calcium fly ash (Class-F FA) using alkali activators [8-9]. However, given the limited availability of metakaolin and the significant added value of high-activity solid waste, there is an increasing interest in exploring cost-effective solid waste substitutes in geopolymer field [10-13]. Current research on single solid waste utilization often follows a linear approach, focusing on individual materials without considering their potential synergistic effects. This limitation will lead to a variety of adverse effects such as low utilization efficiency of solid wastes, limited technological innovation and poor economic benefits [14]. In contrast, multi-component co-utilization offers a promising solution by integrating various solid wastes to enhance material properties and reduce dependence on single sources [15-16]. Sarıdemir et al. [17] studied the synergistic effect of slag and Class-F FA. The concrete with the two solid wastes has a superior frame and better acid/salt resistance. Li et al. [18] utilized Bayer red mud, steel slag, carbide slag, aluminum ash, and flue gas desulfurization gypsum as raw materials to develop high performance red mud-based cementitious materials through the synergistic multi-solid wastes system under high-temperature treatment conditions.

In this research, burnt coal cinder (BCC) and granite powder (GP) were chosen as the basic components for combined disposal. This selection was primarily motivated by the fact that both BCC and GP are solid wastes challenging to manage effectively and could potentially have significant environmental impacts [19]. Additionally, they are not only cost-effective but also possess high silicon and aluminum content along with superior filler properties, suggesting their considerable

potential as geopolymer raw materials. However, due to their stable physical and chemical properties, their reactivity is relatively low. Existing studies indicate that to activate the reaction components in these low-reactive raw materials, it is typically necessary to employ extremely high concentrations of lye [20-23]. For example, Mohapatra et al. [24] and Azimi et al. [25] used more than 20 wt% or extra 22 M alkali activators to prepare geopolymers and the mechanical properties were not outstanding. The extensive use of NaOH inevitably increases the cost and low-activity solid wastes-based geopolymer shows the poor properties. In recent years, many scholars have made efforts to reduce the dosage of alkali activators and improve the low-activity solid wastes-based geopolymer properties through various ways. This includes, but is not limited to, process parameters optimization and cost-effective substitution of Ca activators for traditional NaOH activators [20, 26]. Given this context, the presence of active calcium sources in high-calcium fly ash (Class-C FA) could be a crucial factor in the combined treatment of these two low-activity solid wastes. The use of Class-C FA in the cement industry is restricted due to its elevated CaO content [27]. However, in the field of geopolymers, the unbound CaO can be swiftly hydrated to yield strength. Additionally, CaO and NaOH can synergistically dissolve more reactive aluminosilicate components, thereby increasing the mechanical properties of geopolymers [28].

This paper presents methods for the co-disposal of multi-solid wastes, including BCC, GP, and Class-C FA. To achieve this, response surface methodology (RSM) was employed to optimize the proportion of multi-solid wastes through rigorous

experimentation and statistical analysis [29]. Its successful application in geopolymer production stages facilitates optimal integration of multi-solid wastes, reducing chemical reagent costs and enhancing product performance [30-31]. Based on RSM optimization, a series of single-factor experiments were conducted to further refine process parameters. The optimized geopolymers were characterized using X-ray diffraction (XRD), thermal analysis (TA), Fourier transform infrared spectroscopy (FTIR), and scanning electron microscopy with energy dispersive spectroscopy (SEM-EDS) to clarify the synergistic mechanisms among the multi-solid wastes and highlight the beneficial outcomes of optimal preparation technology. This comprehensive investigation aims to provide a theoretical foundation for pivotal technologies associated with multi-solid waste co-disposal, enhancing the viability of solid wastes resource utilization and contributing to environmental sustainability.

## 2. Experimental materials and methods

### 2.1 Materials

#### 2.1.1 Solid wastes

The BCC and Class-C FA were sourced from the Macheng thermal power plant located in Hubei Province, China. GP was procured from the Macheng stone processing plant in Hubei Province, China. Their primary chemical composition is $SiO_2$ and $Al_2O_3$, with a minor presence of $Fe_2O_3$, CaO, and $K_2O$ (Table 1). The Ca content of Class-C FA approximates 15%, which fulfills the criteria for Class-C FA ($CaO \geq 10\%$) used in the preparation of cement active mixed materials.

The mineral composition of the three raw materials is depicted in Fig. 1(a). BCC

predominantly comprises quartz, mullite, and glass phases. GP also contains significant quantities of quartz and mullite. The Class-C FA exhibits the evident diffraction peak of the Ca component (lime and calcite). Concurrently, Class-C FA is most pronounced at the hump of 15°-30°, indicating its highest content of amorphous substances and activity [32]. This hump is also present in small amounts in BCC, suggesting that the activity of BCC is lower than that of Class-C FA. The least active raw material is GP, which displays a clear peak strength but no discernible hump.

The micro-morphologies of the three raw materials are depicted in Figs. 1(b-d). The BCC predominantly exhibits irregular, massive, and fragmented particles (Fig. 1(b)). The GP contains spherical mineral particles (Fig. 1(c)). Conversely, the Class-C FA is characterized by a substantial presence of glass beads intended to supply active components (Fig. 1(d)).

**Table 1.** Main chemical composition of raw materials (%)

| Chemical composition | $SiO_2$ | $Al_2O_3$ | $Fe_2O_3$ | CaO | $K_2O$ | $Na_2O$ | MgO | Others | LOI |
|---|---|---|---|---|---|---|---|---|---|
| BCC | 53.98 | 30.31 | 4.20 | 1.77 | 0.82 | 0.43 | 0.58 | 1.23 | 6.68 |
| GP | 60.20 | 20.36 | 3.40 | 2.85 | 3.47 | 2.48 | 0.65 | 1.95 | 4.64 |
| Class-C FA | 42.43 | 25.11 | 5.32 | 14.98 | 1.98 | 0.74 | 1.54 | 3.28 | 4.62 |

*Notice: LOI* represents the loss on ignition.

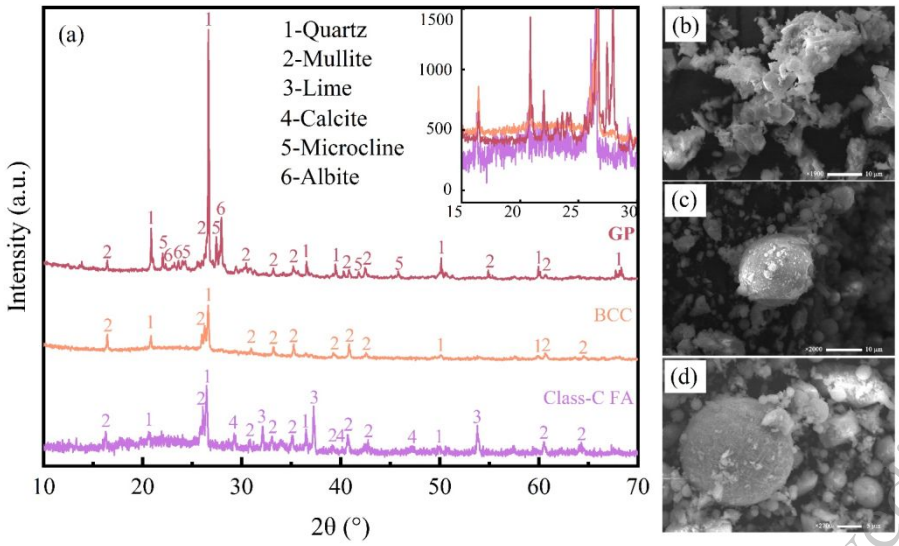


**Fig. 1.** XRD pattern and SEM images of raw materials

2.1.2 Activator

NaOH solution was used as the activator, which was prepared by dissolving NaOH particles (AR, ≥96%) in a certain volume of tap water.

**2.2 Preparation of multi-solid wastes-based geopolymer**

The raw materials were dehydrated by an oven (60°C for 24 h). The dried raw materials were mixed in a certain ratio and ground in a vibrating mill for 1 min to obtain the uniformly dispersed precursor powder. The mass ratio of NaOH to precursor powder was maintained at 1/9, and the ratio of tap water to precursor powder (liquid-solid ratio) was set to 4/15 (mL/g). These conditions had been tentatively demonstrated to yield effective activation outcomes. The slurry was prepared by mixing precursor powder with NaOH solution in the cement slurry mixer. The slurry was poured into plastic molds (20 mm × 20 mm × 20 mm) and vibrated for 1 min to remove the air bubbles. The molds with the slurry were placed in the cement curing box (60°C and 95% RH for 24 h). After that, the geopolymer samples were

taken out of the mold and cured at room temperature.

**2.3 Box-Behnken RSM application**

The statistical software (Design Expert 11) was employed for the design and analysis of the experiment. The Box-Behnken design (BBD) was utilized within Design Expert 11 to investigate the optimal ratio of BCC, GP, and Class-C FA [30, 33]. RSM employs nonlinear fitting model to generate an equation of fit, as depicted in Eq. (1). In this equation, $y$ represents the predicted response, while $\beta_0$, $\beta_i$, $\beta_{ii}$ and $\beta_{ij}$ denote the constant, linear effect, quadratic effect, and interaction effect coefficients respectively. The variables $x_i$ and $x_j$ represent the coded independent factors, k signifies the number of experimental parameters, and ε denotes the random error [34].

$$y = \beta_0 + \sum_{i=1}^{k} \beta_i x_i + \sum_{i=1}^{k} \beta_{ii} x_i^2 + \sum_{j=2}^{k} \sum_{i=1}^{j-1} \beta_{ij} x_i x_j + \varepsilon \quad (1)$$

The BBD includes three factors at three levels, totaling 17 runs: 12 design points and 5 central points for error estimation. Table 2 shows factor levels and coding values. Fig. 2 depicts test points based on coded and actual values of three variables. The 28 d-aged compressive strength of the geopolymer was chosen as the response value, analyzed, and assessed using analysis of variance (ANOVA).



**Table 2.** Levels and factors in BBD

| Levels | Actual factors | | | Code factors | | |
|---|---|---|---|---|---|---|
| | A: BCC | B: GP | C: Class-C FA | $Z_1$ | $Z_2$ | $Z_3$ |
| High | 5 | 2 | 8 | 1 | 1 | 1 |
| 0 | 3 | 1 | 5 | 0 | 0 | 0 |
| Low | 1 | 0 | 2 | -1 | -1 | -1 |

*Notice:* The value of each factor in the table represents its quota in the precursor powder, and the value range is determined by pre-experiment results in section 3.1.

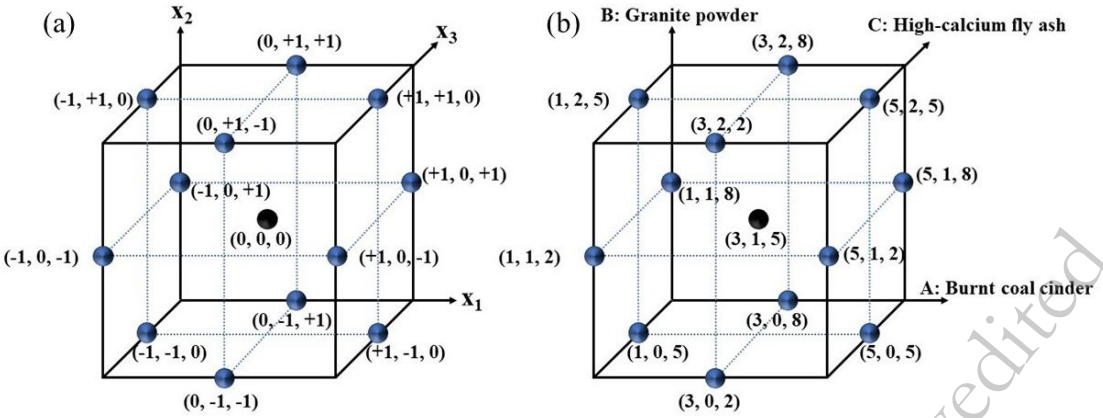


**Fig. 2.** The BBD of geopolymer based on (a) coded and (b) actual values



## 2.4 Characterization and testing

The YAW-100E hydraulic pressure testing machine was employed to assess the 28 d-aged compressive strength of geopolymers, in accordance with GB/T 17671-2021. The mean value derived from five samples was utilized for each set of test results. The geopolymers soaked in acetone for 24 h to halt the hydration reaction. Following the soaking, the geopolymers were dried procedure in an oven at the temperature of 80°C for 24 h. Subsequently, these samples were characterized several times, and the most representative and scientific characterization results were selected for analysis. The phase of the samples under different conditions was analyzed using the XRD (D/MAX-RB), with the scanning range of 10°~70°. The FTIR (Nicolet 6700) was employed to examine the chemical construction of the samples within the wavenumber range of 400~4000 $cm^{-1}$. The microstructure of the samples was observed using the SEM (JSM-IT 300) operating at the voltage of 15 kV. The detailed

analysis of the distribution of elements and the composition of microzone elements was conducted using the EDS (Inca X-Act, Oxford Instruments), with the treatment voltage of 20 kV. TA was performed with a synchronous thermal analyzer (STA, STA449F3) under the condition of nitrogen atmosphere, temperature range: 35~1000℃, and heating rate: 10 ℃/min.

## 3. Results and discussion

### 3.1 Pre-experiment results

RSM experimental design necessitates the reduction of each independent variable's value range through pre-experiments. In Fig. 3, the pre-experiment results show that the highest 28- d-aged compressive strength of geopolymer occurs when the quota of BCC/ GP/ Class-C FA is set to 2/ 1/ 5. The data reveals that geopolymers with higher Class-C FA content generally exhibit superior compressive strength. This further proves that Class-C FA is the most active substance. It is pertinent to observe that excessive incorporation of Class-C FA can also yield negative effects, suggesting that the reasonable matching of multi-solid wastes is very important [35]. After overall consideration, the preliminary value range of RSM for BCC/ GP/ Class-C FA is established as 1-5/ 0-2/ 2-8.

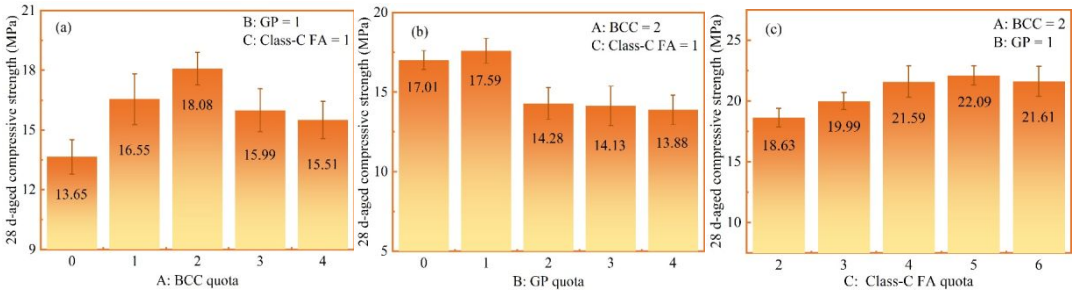

**Fig. 3.** Pre-experiment results of (a) BCC, (b) GP, and (c) Class-C FA

### 3.2 RSM experiment results

The pre-experiments analysis indicates that each factor exerts nonlinear influence on compressive strength, necessitating the use of RSM to elucidate the relationship among these factors. In RSM experiments, the test results for the 28 d-aged compressive strength of geopolymer are presented in Table 3. The BCC/ GP/ Class-C FA quota is set to 1/ 1/ 8, with the maximum 28 d-aged compressive strength reaching 27.79 MPa. Obviously, the addition of BCC and GP is obviously limited due to their lower activity.

**Table 3.** Design plans and results of RSM

| Std. | Run | Factor A | Factor B | Factor C | Response |
|---|---|---|---|---|---|
| | | BCC | GP | Class-C FA | 28 d-aged compressive strength (MPa) |
| 1 | 16 | 1 | 0 | 5 | 26.05 |
| 2 | 17 | 5 | 0 | 5 | 23.14 |
| 3 | 9 | 1 | 2 | 5 | 25.78 |
| 4 | 15 | 5 | 2 | 5 | 22.14 |
| 5 | 11 | 1 | 1 | 2 | 24.73 |
| 6 | 4 | 5 | 1 | 2 | 21.46 |
| 7 | 6 | 1 | 1 | 8 | 27.79 |
| 8 | 8 | 5 | 1 | 8 | 26.54 |
| 9 | 2 | 3 | 0 | 2 | 22.86 |
| 10 | 14 | 3 | 2 | 2 | 21.41 |
| 11 | 13 | 3 | 0 | 8 | 26.43 |

| | | | | | |
|---|---|---|---|---|---|
| 12 | 3 | 3 | 2 | 8 | 25.11 |
| 13 | 10 | 3 | 1 | 5 | 26.82 |
| 14 | 1 | 3 | 1 | 5 | 26.45 |
| 15 | 5 | 3 | 1 | 5 | 27.14 |
| 16 | 12 | 3 | 1 | 5 | 26.58 |
| 17 | 7 | 3 | 1 | 5 | 27.29 |



### 3.3 RSM model significance and applicability

#### 3.3.1 ANOVA for significance

The statistical analysis was conducted on the experimental data, with the general model equation presented in Eq. (2). The significance of the model was assessed using ANOVA, as detailed in Table 4. The lack of fit is not significant and the model's F-value stands at 39.68. Both these indicators suggest that the model possesses statistical significance. Generally, variables with p-value less than 0.1 are deemed effective, and those with p-value less than 0.05 are considered significant [36]. As can be observed from Table 4, all single factors have p-values less than 0.05, suggesting that all single factors were statistically significant at the 95% confidence level. The factors that significantly influence compressive strength can be ranked as follows: C > A > B. The ordering precisely aligns with the sequence of activity levels observed for each raw material (Fig. 3 and Table 3), underscoring the most importance of activity in influencing the properties of geopolymers.

The results of the model verification are presented in Table 5. The discrepancy between the Pred-$R^2$ of 0.7936 and the Adj-$R^2$ of 0.9561 is less than 0.2, suggesting a strong correlation between the actual and predicted values and high degree of fit. The

coefficient of variation (C.V.) serves as an indicator of the accuracy of the experiment. Lower C.V.% signifies higher reliability. The C.V.% is 1.78% (less than 5%), suggesting that the experimental operation is reliable [37]. Adeq. precision is a measure of the signal-to-noise ratio, with the ratio greater than 4 being desirable. The ratio of 19.285 in this study suggests an adequate signal.

$$Y_{28d}=20.97+0.03\times A+3.47\times B+1.52\times C-0.09\times AB+0.08\times AC+0.01\times BC-0.18\times A^2-1.88\times B^2-0.11\times C^2 \quad (2)$$

**Table 4.** ANOVA of RSM model

| Source | Sum of Squares | df | Mean Square | F-value | p-value | Significance |
|---|---|---|---|---|---|---|
| Model | 71.53 | 9 | 7.95 | 39.68 | < 0.0001 | Significant |
| A- BCC | 15.32 | 1 | 15.32 | 76.47 | < 0.0001 | |
| B-GP | 2.04 | 1 | 2.04 | 10.18 | 0.0152 | |
| C- Class-C FA | 29.68 | 1 | 29.68 | 148.17 | < 0.0001 | |
| AB | 0.1332 | 1 | 0.1332 | 0.6650 | 0.4416 | |
| AC | 1.02 | 1 | 1.02 | 5.09 | 0.0586 | |
| BC | 0.0042 | 1 | 0.0042 | 0.0211 | 0.8886 | |
| $A^2$ | 2.07 | 1 | 2.07 | 10.31 | 0.0148 | |
| $B^2$ | 14.85 | 1 | 14.85 | 74.13 | < 0.0001 | |
| $C^2$ | 4.43 | 1 | 4.43 | 22 .10 | 0.0022 | |
| Residual | 1.40 | 7 | 0.2003 | | | |
| Lack of Fit | 0.8910 | 3 | 0.2970 | 2.32 | 0.2165 | Not significant |
| Pure Error | 0.5113 | 4 | 0.1278 | | | |
| Cor Total | 72.93 | 16 | | | | |

**Table 5.** Validation results of RSM model

| Response | $R^2$ | Adj-$R^2$ | Pred-$R^2$ | C.V. % | Adeq. precision | Lack of fit | Significance |
|---|---|---|---|---|---|---|---|
| 28 d-aged compressive strength | 0.98 | 0.95 | 0.79 | 1.78 | 19.28 | not significant | significant |

3.3.2 Diagnostic analysis for applicability

To validate the applicability of model for experimental data, Fig. 4 presents diagnostic plots of quadratic response surface regression model. Outliers in diagnostic plots serve to denote the magnitude of residuals and validate if any data possessed particularly large residuals [38]. Fig. 4(a) presents data distribution characteristic and sufficiency [39]. The point distribution for all dependent variables is nearly entirely linear, suggesting that the residual adheres to normal distribution and the error term are relatively independent. The plots of Figs. 5(b-c) reveal that points are randomly scattered between -4.8 and +4.8, centered around zero on the outlier T axis. This suggests that the variance in the 28 d-aged compressive strength of multi-solid wastes-based geopolymers remain relatively consistent. There is no violation of the assumptions of independence or constant variance across all runs [40]. To verify the fit between the model and experimental data, the scatter plot is constructed with the actual value as the abscissa and the predicted value as the ordinate, as shown in Fig. 4(d). All points are nearly distributed along the straight line, indicating that the actual values align well with the predicted values, and the model can predict test results with high precision.

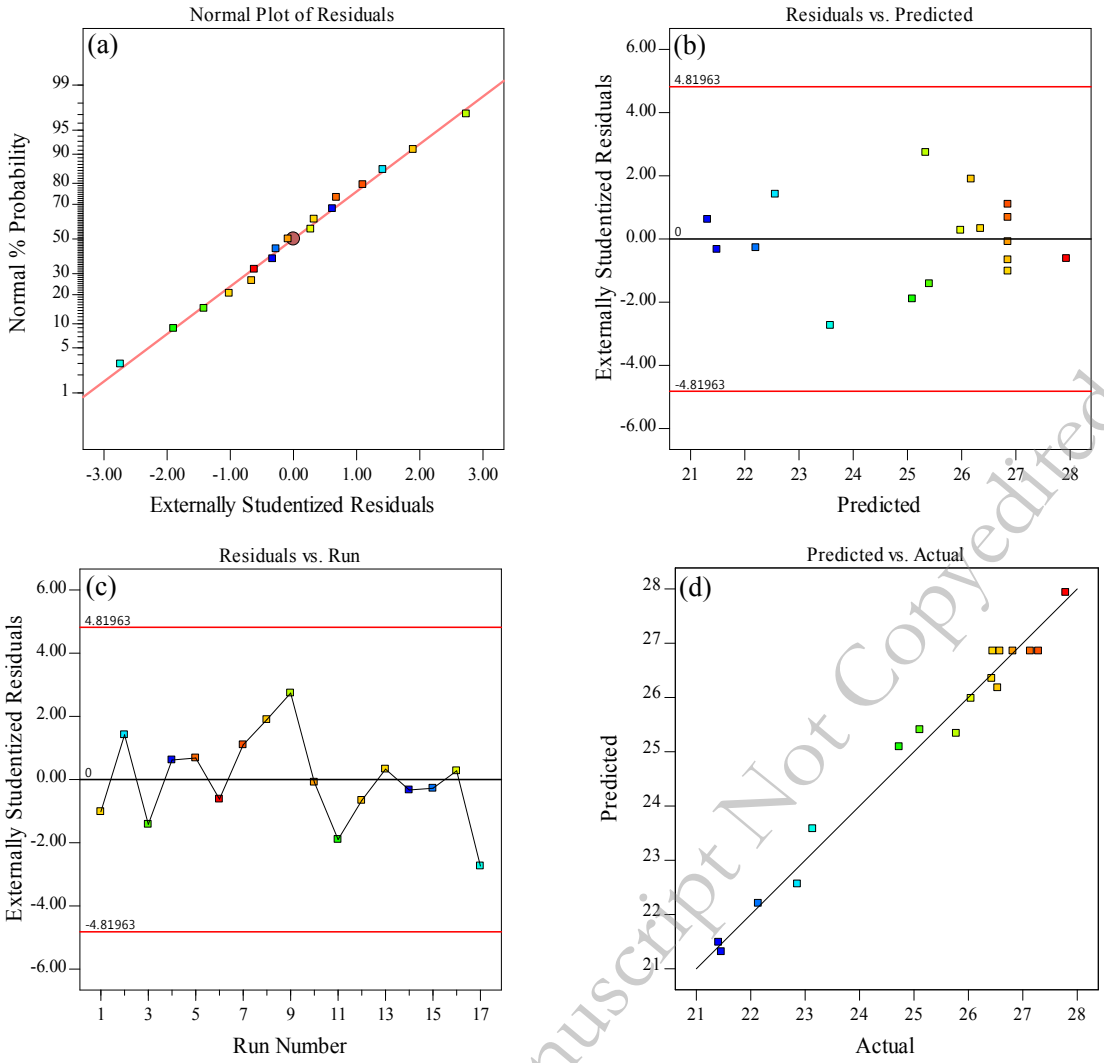


**Fig. 4.** Diagnostic plots of quadratic response surface regression model: (a) Normal probability against externally studentized residuals, (b) Externally studentized residuals against predicted, (c) Externally studentized residuals against run number, and (d) Predicted against actual



## 3.4 RSM analysis and process optimization

### 3.4.1 RSM analysis

Fig. 5 shows the 3D-response surface provides representation of the influence of two factors on the response value. The curvature of the 3D-response surface is indicative of significance of factor interactions [41]. Fig. 5(a) illustrates the effect of variations in BCC and GP content on the 28 d-aged compressive strength at a fixed

amount of Class-C FA. The 3D-response surface exhibits a continuous convex shape and a distinct optimal range. The optimal quotas of BCC to GP does not exceed 2, suggesting that the performance requirements of geopolymer significantly constrain the content of low-activity raw materials. Fig. 5(b) illustrates the optimal performance of the geopolymer is observed when the quota of Class-C FA is approximately 7. This suggests that Class-C FA significantly contributes to the enhancement of performance across multi-solid wastes-based geopolymer. Moreover, the strength contribution of Class-C FA on geopolymer is again reflected in the Fig. 5(c). This is because the Class-C FA containing high-active component will produce a large number of gel substances, which is the foundation for optimizing the physical properties of geopolymers [42].

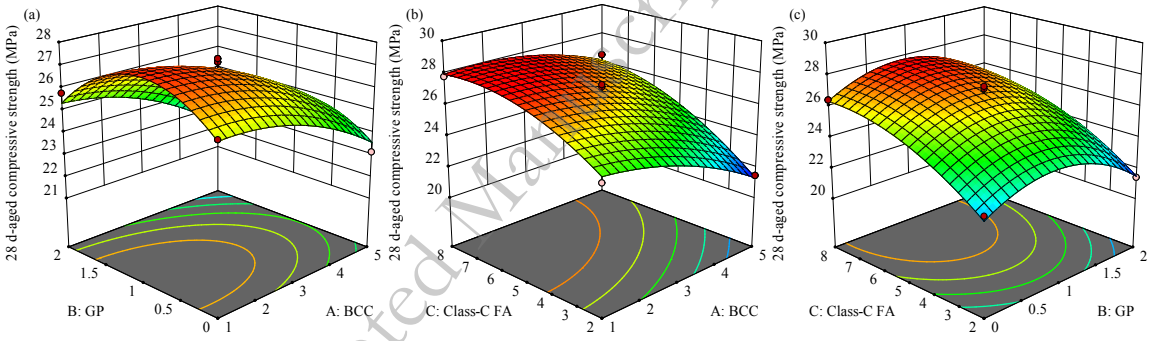


**Fig. 5.** 3D-response surface on compressive strength of 28 d-aged geopolymers

Numerical multi-objective optimization technique, response surface fitting model and expectation function were used to maximize the geopolymer compressive strength. The content range of BCC/ GP/ Class-C FA was set to 1-5/ 0-2/ 2-8, and the maximum compressive strength range was set to 25-35 MPa. Through RSM optimization, the only specified scheme was given as BCC: GP: Class-C FA = 1.6:

0.9: 7.3, and the predicted compressive strength was 28.10 MPa. The test was carried out according to the above raw material ratio. The actual average compressive strength of the prepared geopolymer was 29.24 MPa. Their error was less than 5%, so the optimization was effective. Following the RSM optimization, the 28 d-aged compressive strength of the multi-solid wastes-based geopolymer exhibited an enhancement of approximately 27% in comparison to its pre-optimization state.

3.4.2 Process optimization

Following the precise determination of the optimal raw material ratio through RSM, further optimization adjustments were implemented for other pivotal parameters within the process flow, as depicted in Fig. 6. Specifically, a series of single-factor experiments adjusted the mass ratio of NaOH-precursor powder to 0.084, while the liquid-solid ratio was established at 0.222. The mixture slurry was subsequently cured for 24 h at a consistent temperature of 80°C. The high-compressive strength geopolymer was successfully prepared upon further curing at room temperature for 27 d. The 28 d-aged compressive strength of this multi-solid wastes-based geopolymer achieved a remarkable 61.34 MPa.

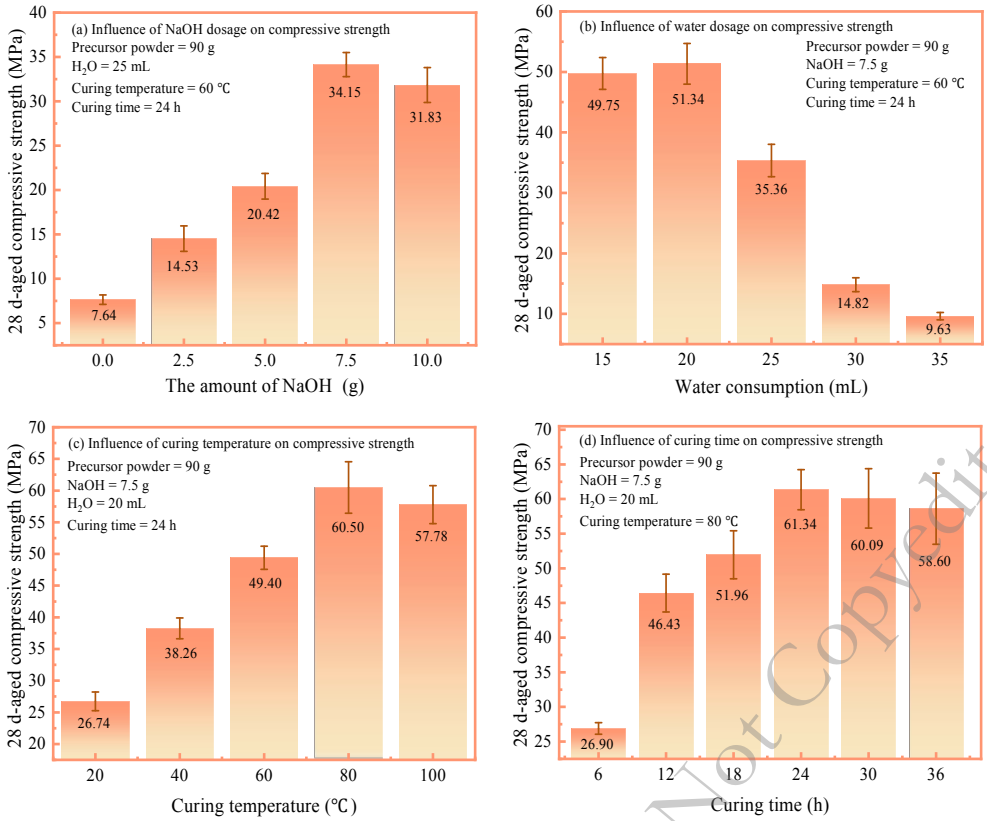


**Fig. 6.** Process parameters optimization through single-factor experiments

By comparing the study with existing research results (Table 6), the studied geopolymer shows significant advantages in terms of compressive strength and dosage of activator. Specifically, the optimized product not only reduces the amount of activator but also achieves efficient activation of low-reactive raw materials. The optimized geopolymer products successfully reached the 52.5R strength grade specified in GB 175-2023. While maintaining high performance, it further enhances cost-effectiveness and environmental protection characteristics.

**Table 6.** Comparison of product properties and dosage of activators

| Products | Raw materials | Dosage of activators (wt%) | 28 d-aged Compressive | Reference |
|---|---|---|---|---|

| | | | strength (MPa) | |
|---|---|---|---|---|
| Geopolymer | BCC/GP/Class-C FA | NaOH (8.4) | 61.34 | This research |
| Geopolymer | GP | $Na_2SiO_3$+NaOH (20) | 22.00 | [24] |
| Geopolymer | Dolomite/FA | $Na_2SiO_3$+NaOH (35.2) | 46.38 | [25] |
| Brick | Class-C FA/Brick powder | $Na_2SiO_3$+NaOH (20) | 44.20 | [43] |
| Ceramic | Coal gangue | $Na_2SiO_3$+NaOH (20.1) | 19.00 | [44] |



**3.5 Mechanism analysis and discussion**

3.5.1 Comparative experimental design

To study the contribution of three solid wastes to geopolymerization and determine the synergistic mechanism among them. Three groups with high BCC content (GBCC), high GP content (GGP), and high Class-C FA content (GFA) were selected to compare with the RSM-optimization group (GRSM). Their mass ratios of BCC, GP, and Class-C FA are as follows: 5: 1: 2, 2: 5: 1, 1: 2: 5, and 1.6: 0.9: 7.3, respectively. All other experimental conditions were kept constant to that of the RSM-optimization group. The compressive strength for each group is presented in Fig. 7. The RSM-optimization group exhibits significantly higher compressive

strength than the other three groups. The role of each component in the geopolymerization process will be elucidated later, in conjunction with the test analysis.

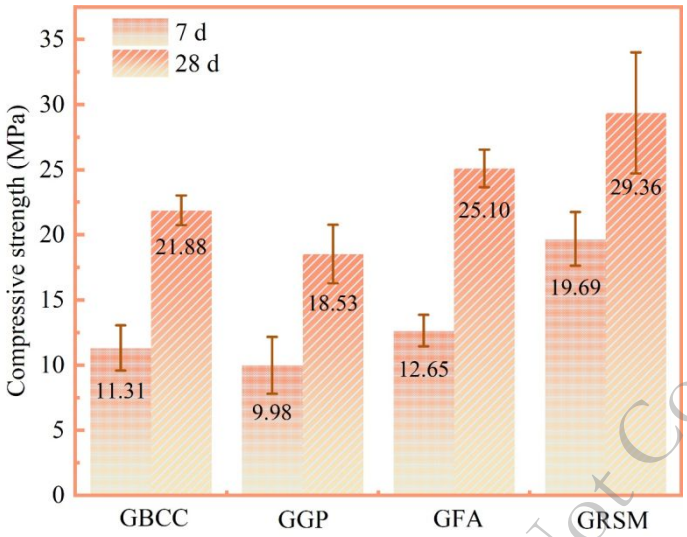


**Fig. 7.** The compressive strength of comparative experimental

3.5.2 XRD and TA analysis

The XRD patterns of geopolymers with varying proportions are depicted in Fig. 8(a). The intensity of quartz diffraction peaks in the four groups of experiments is different. It is weakest in GRSM and strongest in GGP. This variation corresponds to the characteristic of raw materials used. Specifically, an increase in GP significantly enhances the inert quartz diffraction peak (Fig.1). This observation corresponds to the compressive strength value of Fig. 7, which confirms the significant limitation of inert mineral content on the mechanical properties of geopolymers [45].

As illustrated in GBCC, the formation of analcime can occur under conditions of high BCC content. This compound, the stable zeolite structure with low Si content [46], contributes to the stability of the geopolymer [47]. However, the excessively

high BCC content cannot result in a significant formation of analcime and its quartz peak ranks second only to GGP. These are also an important reason why the compressive strength is limited. Within GGP, elevated GP content not only contributes to a relatively larger proportion of the inert quartz but also introduces the new inert albite [48]. This indicates that the geopolymerization activity of GP is significantly low, and the geopolymer also contains more inert minerals rather than amorphous gels. This is also the main reason for the lowest compressive strength of the high GP content.

In GFA and GRSM, anorthite [49] and wairakite [50] with Ca components are found respectively. Anorthite behaves as an inert mineral phase akin to albite, whereas wairakite functions in a similar manner to analcime. The primary factor contributing to the markedly lower compressive strength observed in GFA compared to GRSM is the substantial incorporation of high-calcium active substances, which triggers the formation of an inert Ca-containing mineral phase (anorthite). This phenomenon significantly influences the mechanical properties of the geopolymer within GFA. In the GRSM, the optimal ratio after RSM optimization avoids the formation of inert by-products and improves the production of Ca-containing zeolite minerals (wairakite). The paramount reason for the positive impact following RSM optimization lies in its ability to drive low-activity components through the high-activity components, while concurrently ensuring beneficial geopolymerization products. This synergistic effect optimizes the overall performance of multi-solid wastes-based geopolymer.

The analysis of mass loss at specific temperatures further confirmed the positive effect of RSM optimization (Figs. 8(b-d)). Thermogravimetry (TG) revealed three stages of mass loss: the first stage (I) occurred between 40℃ and 320℃, primarily due to the evaporation of adsorbed water and bound water; the second stage (II) ranged from 320℃ to 620℃, corresponding to the digestion of impurities such as unburned carbon and pollutants in solid waste; the third stage (III) occurred between 620℃ and 1000℃, resulting from the decomposition of carbonate [51]. In the stage I, GGP exhibited the least mass loss at only 5.79%, attributed to the minimal gel phase content and the absence of adsorbed water from albite (Fig. 8(a)). Conversely, the mass loss of GBCC, GFA, and GRSM were primarily associated with the dehydration process of N-(C)-A-S-H gels or Ca-containing zeolite by-products. In stage II, GFA demonstrated the most significant weight loss (2.45%), indicating that the performance decline of adding a large amount of highly active Class-C FA was due to the formation of a high content of uncertain impurities. This consistent with the observation of Fig. 8(a) that the reaction direction of GFA is not controlled, forming the inert Ca-containing anorthite. However, GRSM exhibited the least mass loss in this interval, further suggesting that RSM optimization may effectively reduce the generation of useless impurities after reaction by promoting synergy.

In the derivative thermogravimetry (DTG) curve, GGP exhibited a shoulder peak phenomenon at 110.1℃ and 159.3℃, whereas other groups predominantly displayed a single peak. This behavior is primarily attributed to the interlayer structure of the gel and the pore structure of Ca-containing zeolite by-products. They increase the binding

of adsorbed water, so that the loss temperature range of adsorbed water is closer to that of bound water [52-53]. In GGP, due to the minimal amount of gel and the presence of albite by-products, there was a noticeable split in the loss temperature range of adsorbed water and bound water [54]. In the differential scanning calorimetry (DSC) curve, GFA and GRSM exhibit a high degree of coincidence. Their exothermic peaks consistently appear near 800°C, which is likely attributable to the carbonization of Class-C FA and sodium hydroxide in the presence of air during the hydration reaction [55]. Furthermore, four groups display exothermic peak around the high temperature of 285℃. This suggests that, in comparison to adsorbed water, the bound water of the gel phase is more prevalent. Consequently, all groups contain a certain quantity of gel products.

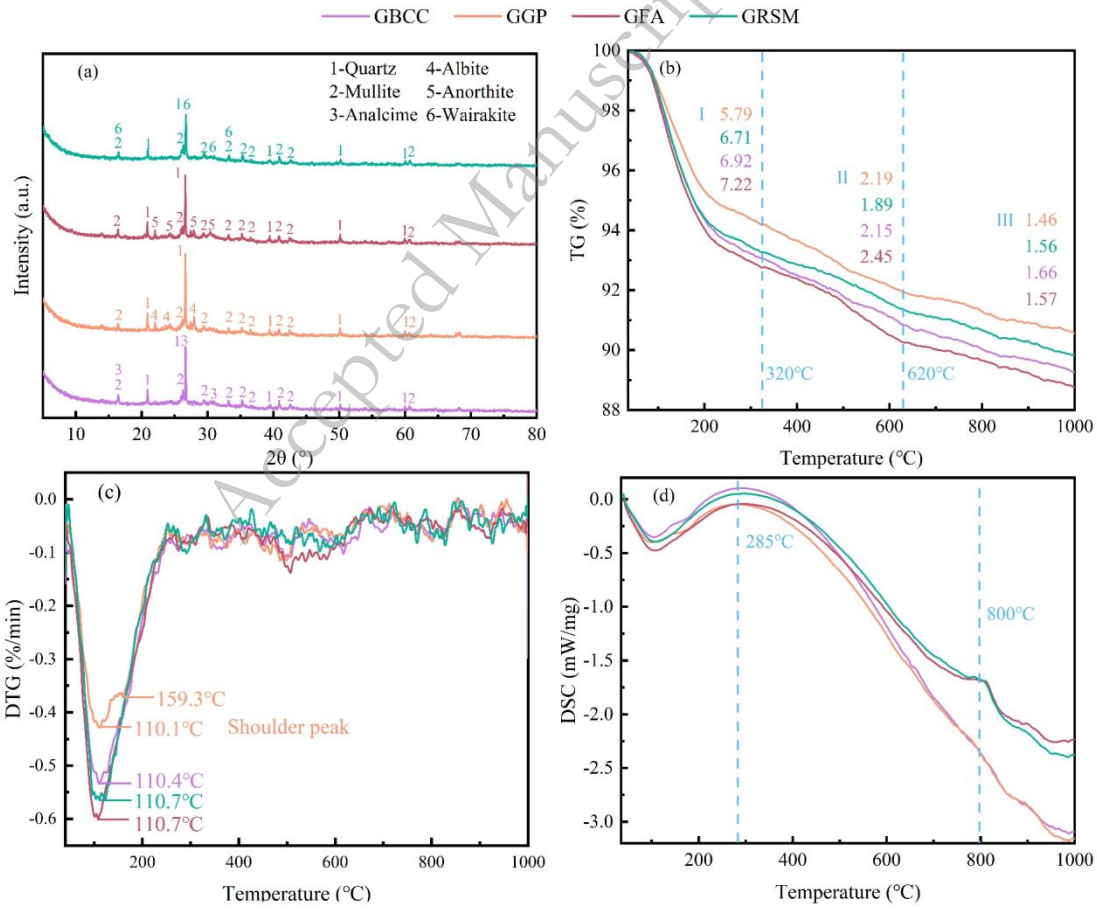

**Fig. 8.** XRD patterns and TA diagram of 28 d-aged geopolymers

3.5.3 FTIR analysis

The FTIR spectra of 28d-aged geopolymer prepared with four different ratios are depicted in Fig. 9. The $t_{OH}$ and $d_{OH}$ vibration zones at 3400 $cm^{-1}$ and 1640 $cm^{-1}$ indicate the presence of hydration products. The symmetric stretching of Si-O-Al at 566 $cm^{-1}$ confirms the existence of mullite. The T-O (T =Si, Al) bending vibrations are observed at 460 $cm^{-1}$, and this band is used to determine the degree of amorphization of the material [56]. The absorption band at 1456 $cm^{-1}$ is ascribed to the tensile vibration of O-C-O, which is associated with the carbonization process in the geopolymerization [57]. This absorption band is associated with the mass loss observed during the thermogravimetric stage III (Fig. 8(b)). The extent of carbonation in the geopolymerization serves as an indirect indicator of the precursor powder activity. The characteristic peaks of Si-O-T within the 900-1100 $cm^{-1}$ range serve as indicators for the formation of three-dimensional aluminum silicate network of gels [58]. The main absorption bands of GFA and GRSM at 900-1100 $cm^{-1}$ shift towards lower wavenumber, signifying an elevated content of Al substituting Si. This observation reaffirms the high activity of Class-C FA, which can yield more gels. The characteristic enables it to serve as the primary source of the gel substance in the geopolymer, while other solid wastes primarily function as supplementary materials to optimize the structure of geopolymer.

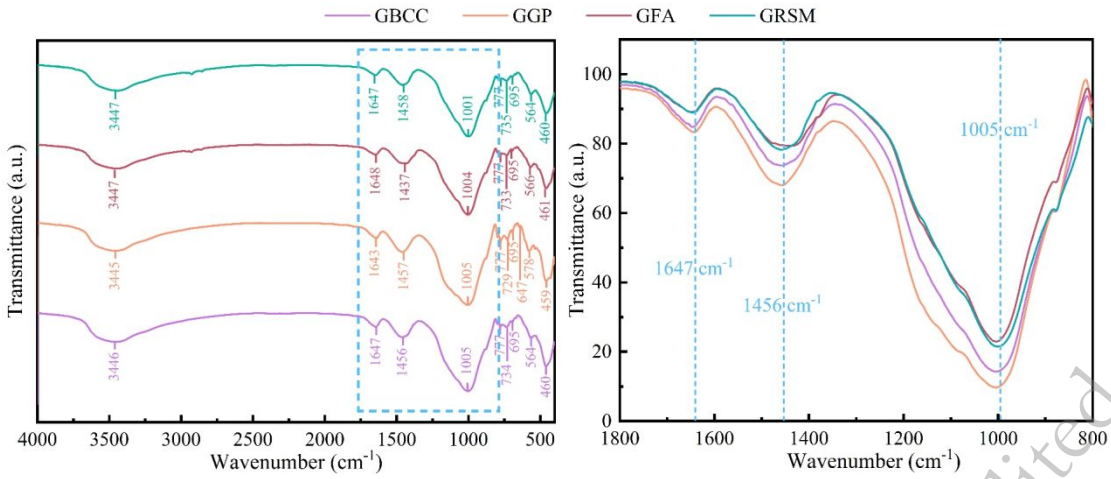


**Fig. 9.** FTIR spectra of 28 d-aged geopolymers

3.5.4 SEM-EDS analysis

Fig. 10 shows microscopic images of the geopolymer fracture surface with four different groups. Fig. 10(a) shows that a significant number of unreacted particles are embedded within GBCC matrix on the crack surface. This suggests that while there is certain amount of gels, it is insufficient to entirely envelop the unreacted particles. Conversely, Fig. 10(b) illustrates the extensive dimples caused by particles spalling in GGP. The content of active ingredients in GP is markedly deficient, leading to diminished gels and subsequently reducing the adhesion of particles. In Fig. 10(c), it is noted that the matrix of GFA exhibits fewer micro-cracks and relatively dense microstructure. However, a significant number of gel-like coated particles formed clusters, which indicates that the distribution of the gel is markedly uneven. This adversely affects the overall bonding efficacy of the geopolymer. Fig. 10(d) is the microscopic image of the GRSM with the optimal ratio of solid wastes. Although some micro-cracks are still exposed on the matrix surface, the integrity of the geopolymer matrix can now be clearly observed, with uniform distribution of gel and

particles interlacing and bonding with each other. This indicates that the synergistic effect of multi-solid wastes after RSM optimization has a significant gain in structure.

From the comparison of the distribution of the four groups of elements, it can be found that the distribution of GRSM elements is more uniform. This further substantiates that the geopolymer structure, optimized using the RSM, exhibits greater compact and uniformity. The synchronous dense distribution of Ca and gel products is due to the substitution of Na by Ca. This substitution leads to the formation of hybrid gel (N-(C)-A-S-H) during the geopolymerization. It is noteworthy that the black area at the top of the GRSM is consequence of the diminished signal intensity in this region, which is attributed to the substantial disparity in sample height. In contrast, the distribution of other groups' elements exhibited significant degree of aggregation and unevenness, characterized by pronounced highlighted and dark areas. The comparison of EDS scanning results further confirms the result that RSM optimization can evenly distribute gels and fillers to enhance the physicochemical properties of geopolymers by producing sufficient gels and reducing the negative effects of Ca.

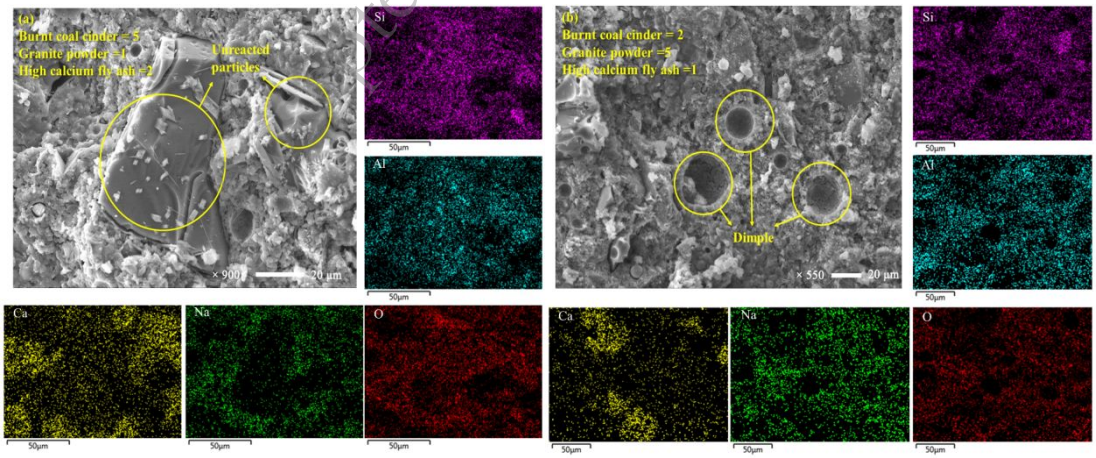

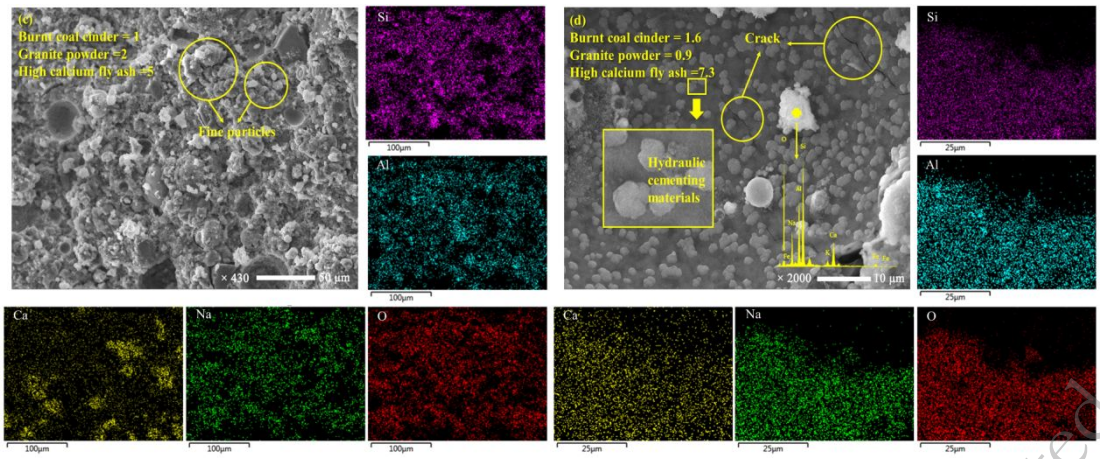


**Fig. 10.** Microstructure and element distribution images of 28 d-aged geopolymers

## 4. Conclusion

This study investigated the critical process parameters for preparation high-performance geopolymers using burnt coal cinder (BCC), granite powder (GP), and high-calcium fly ash (Class-C FA) as raw materials, with NaOH serving as an activator. According to the response surface methodology (RSM), the influence degree of each raw material on the multi-solid wastes-based geopolymer was determined as Class-C FA > BCC > GP, and the respective ratio was precisely adjusted. On this basis, the dosage of activator, liquid-solid ratio and curing conditions were systematically optimized through single-factor experiments. When the mass ratio of BCC, GP, and Class-C FA is set to 1.6: 0.9: 7.3, and the mass ratio of NaOH to the precursor powder is adjusted to 0.084, using the liquid-solid ratio of 0.222 under the defined curing conditions (80°C for 24 h and then room temperature for 27 d), the prepared geopolymers shows superior compressive strength of 61.34 MPa. This significantly exceeds the national standard GB 175-2023 with strength grade of 52.5R, demonstrating its substantial potential as building materials.

Class-C FA possesses high Ca content that significantly accelerates the geopolymerization. This results in the formation of unique hybrid N-(C)-A-S-H gel, which substantially enhances the microstructural density and overall mechanical properties of the material. However, solely relying on class-C FA leads to uncontrolled hydration and direction, accompanied by the uneven distribution of hybrid gels. BCC can effectively modulate the Ca content while maintaining a certain level of activity in the precursor powder. Furthermore, the judicious addition of GP can optimize the size distribution of geopolymers, thereby enhancing their structural density. Following RSM optimization of multi-solid wastes, the significant improvement in gel phase richness and structural homogenization is achieved. Accumulation of these microstructural changes culminates in the successful preparation of geopolymer materials exhibiting ultra-high compressive strength.

In conclusion, the engineering optimization of multi-solid wastes-based geopolymer necessitates the exploration and selection of alkaline solid wastes that can provide a similar alkaline environment. This can reduce the need for activators and lowering costs. Concurrently, it is crucial to conduct an in-depth analysis of the physicochemical characteristics of various types of solid waste to facilitate their adaptive collaboration in specific application scenarios. Furthermore, the RSM is an effective strategy to enhance the comprehensive properties of geopolymers. In industrial settings, the developed multi-solid wastes-based geopolymers can be extensively used in construction, roads, bridges, and other fields as a powerful alternative to traditional materials such as cement and concrete. This provides

superior strength and durability and contributes to the sustainable development of related industries.

**Acknowledgments**

This work was supported by the Key Research and Development Program of Hubei Province (2022BAA029) and the Major Project of Metallurgical Corporation of China Limited.

**References**

[1] J.C. Lao, R.Y. Ma, L.Y. Xu, et al., Fly ash-dominated high-strength engineered/strain-hardening geopolymer composites (HS-EGC/SHGC): influence of alkalinity and environmental assessment, J. Clean. Prod., 447(2024), art. No. 141182. https://doi.org/10.1016/j.jclepro.2024.141182.

[2] C. Miao, L.X. Liang, F. Zhang, et al., Review of the fabrication and application of porous materials from silicon-rich industrial solid waste, Int. J. Miner. Metall. Mater., 29(2022), No. 3, p. 424-438. https://doi.org/10.1007/s12613-021-2360-9.

[3] L.N. Assi, K. Carter, E. Deaver, and P. Ziehl, Review of availability of source materials for geopolymer/sustainable concrete, J. Clean. Prod., 263(2020), art. No. 121477. https://doi.org/10.1016/j.jclepro.2020.121477.

[4] C.F. Xin, S.X. Bao, Y.M. Zhang, et al., Selective leaching mechanisms of zinc from industrial waste using hybrid acids: Sustainable synthesis of Nano-ZnO, J. Environ. Manage., 373(2025), art. No. 123528. https://doi.org/10.1016/j.jenvman.2024.123528.

[5] M. Rodchom, P. Wimuktiwan, K. Soongprasit, et al., Preparation and characterization of ceramic materials with low thermal conductivity and high strength using high-calcium fly ash, Int. J. Miner. Metall. Mater., 29(2022), No. 8, p. 1635-1645. https://doi.org/10.1007/s12613-021-2367-2.

[6] Q. Zhang, B. Liu, K. Xiao, et al., Preparation and hydration of industrial solid waste-cement blends: A review, Int. J. Miner. Metall. Mater., 29(2022), No. 12, p. 2106-2116. https://doi.org/10.1007/s12613-022-2538-9.

[7] B. Ren, Y.L. Zhao, H.Y. Bai, et al., Eco-friendly geopolymer prepared from solid wastes: A critical review, Chemosphere, 267(2021), art. No. 128900. https://doi.org/10.1016/j.chemosphere.2020.128900.

[8] M.N.S. Hadi, M. Al-Azzawi, and T. Yu, Effects of fly ash characteristics and alkaline activator components on compressive strength of fly ash-based geopolymer mortar, Constr. Build. Mater., 175(2018), p. 41-54. https://doi.org/10.1016/j.conbuildmat.2018.04.092.

[9] A. Oz, B. Bayrak, E. Kavaz, et al., The radiation shielding and microstructure properties of quartzic and metakaolin based geopolymer concrete, Constr. Build. Mater., 342(2022), art. No. 127923. https://doi.org/10.1016/j.conbuildmat.2022.127923.

[10] A.L. Almutairi, B.A. Tayeh, A. Adesina, et al., Potential applications of geopolymer concrete in construction: A review, Case Stud. Constr. Mat., 15(2021), art. No. e00733. https://doi.org/10.1016/j.cscm.2021.e00733.

[11] W. Ding, S.X. Bao, Y.M. Zhang, et al., Stepwise recycling of valuable metals

from spent lithium-ion batteries based on in-situ thermal reduction and ultrasonic-assisted water leaching, Green Chem., 25(2023), No. 17, p. 6652-6665. https://doi.org/10.1039/d3gc01673k.

[12] W. Ding, S.X. Bao, Y.M. Zhang, et al., Sustainable regeneration of high-performance cathode materials from spent lithium-ion batteries through magnetic separation and coprecipitation, J. Clean. Prod., 438(2024), art. No. 140798. https://doi.org/10.1016/j.jclepro.2024.140798.

[13] Q. Zhang, B. Liu, K. Xiao, et al., Preparation and hydration of industrial solid waste-cement blends: A review, Int. J. Miner. Metall. Mater., 29(2022), No. 12, p. 2106-2116. https://doi.org/10.1007/s12613-022-2538-9.

[14 Y. Shao, S.L. Ma, S.Y. Li, et al., Low carbon research in precast concrete based on the synergistic mechanism of red mud-ground granulated blast furnace slag powder, J. Clean. Prod., 439(2024), art. No. 140882. https://doi.org/10.1016/j.jclepro.2024.140882.

[15] X.X. Zhou, and J.M. Shen, Micromorphology and microstructure of coal fly ash and furnace bottom slag based light-weight geopolymer, Constr. Build. Mater., 242(2020), art. No. 118168. https://doi.org/10.1016/j.conbuildmat.2020.118168.

[16] Z.M. Qiu, S.X. Bao, Y.M. Zhang, et al., Effect of Portland cement on the properties of geopolymers prepared from granite powder and fly ash by alkali-thermal activation, J. Build. Eng., 76 (2023), art. No. 107363. https://doi.org/10.1016/j.jobe.2023.107363.

[17] M. Sarıdemir, and S. Çelikten, Effect of high temperature, acid and sulfonate on

properties of activated lightweight aggregate concrete, Constr. Build. Mater., 317(2022), art. No. 125886. https://doi.org/10.1016/j.conbuildmat.2021.125886.

[18] Z.F. Li, J. Zhang, S.C. Li, et al., Feasibility of preparing red mud-based cementitious materials: Synergistic utilization of industrial solid waste, waste heat, and tail gas, J. Clean. Prod., 285(2021), art. No. 124896. https://doi.org/10.1016/j.jclepro.2020.124896.

[19] J.J. Zhang, X.Y. Zhang, B. Liu, et al., Phase evolution and properties of glass ceramic foams prepared by bottom ash, fly ash and pickling sludge, Int. J. Miner. Metall. Mater., 29(2022), No. 3, p. 563-573. https://doi.org/10.1007/s12613-020-2219-5.

[20] M.Y. Huang, S.X. Bao, Y.M. Zhang, et al., Calcium-activated geopolymer ceramics: Study of powder calcination and amorphous gel phases, J. Am. Ceram. Soc., 106(2023), No. 6, p. 3964-3977. https://doi.org/10.1111/jace.19052.

[21] I.D.S. Dos Santos, S.X. Bao, and M.Y. Huang, Mechanical and microstructural properties analysis of one-part geopolymer based on burnt coal cinder replaced by metakaolin, J. Build. Eng., 76(2023), art. No. 107265. https://doi.org/10.1016/j.jobe.2023.107265.

[22] M.Y. Huang, S.X. Bao, Y.M. Zhang, et al., The combined effects of calcium oxide and phosphate on burnt coal cinder-based cementitious materials, Constr. Build. Mater., 362(2023), art. No. 129720. https://doi.org/10.1016/j.conbuildmat.2022.129720.

[23] L.X. Jia, M. Huang, M.Y. Huang, et al., Preparation of granite powder-based

geopolymer by synergistic action of calcination and phosphoric acid, J. Am. Ceram. Soc., 107(2024), No. 1, p. 501-513. https://doi.org/10.1111/jace.19422.

[24] M. Nadeem, S. Ilyas, E. Ul Haq, et al., Improved water retention and positive behavior of silica based geopolymer utilizing granite powder, Silicon, 14(2022), No. 5, p. 2337-2349. https://doi.org/10.1007/s12633-021-01047-x.

[25] E.A. Azimi, M. Salleh, M.M.A. Abdullah, et al., Effect of NaOH molar concentration on microstructure and compressive strength of dolomite/fly ash-based geopolymers, Arch. Metall. Mater., 67(2022), No. 3, p. 993-998. https://doi.org/10.24425/amm.2022.139693.

[26] B. Nanda, S.S. Mohapatra, J. Mishra, and S.K. Patro, A review on waste-derived alkali activators for preparation of geopolymer composite, Mater. Today: Proc., 56(2022), p. 440-446. https://doi.org/10.1016/j.matpr.2022.01.400.

[27] D. Pushpalal, S. Danzandorj, N. Bayarjavkhlan, et al., Compressive strength development and durability properties of high-calcium fly ash incorporated concrete in extremely cold weather, Constr. Build. Mater., 316(2022), art. No. 125801. https://doi.org/10.1016/j.conbuildmat.2021.125801.

[28] S. Hanjitsuwan, S. Hunpratub, P. Thongbai, et al., Effects of NaOH concentrations on physical and electrical properties of high calcium fly ash geopolymer paste, Cem. Concr. Compos., 45(2014), p. 9-14. https://doi.org/10.1016/j.cemconcomp.2013.09.012.

[29] B.W. Chong, R. Othman, R.P. Jaya, et al., Design of experiment on concrete mechanical properties prediction: A critical review, Materials, 14(2021), No. 8, p.

1866. https://doi.org/10.3390/ma14081866.

[30] X.S. Shi, C. Zhang, X.Q. Wang, et al., Response surface methodology for multi-objective optimization of fly ash-GGBS based geopolymer mortar, Constr. Build. Mater., 315(2022), art. No. 125644. https://doi.org/10.1016/j.conbuildmat.2021.125644.

[31] L.Z. Guo, M. Zhou, X.Y. Wang, et al., Preparation of coal gangue-slag-fly ash geopolymer grouting materials, Constr. Build. Mater., 328(2022), art. No. 126997. https://doi.org/10.1016/j.conbuildmat.2022.126997.

[32] M.G.S. Ribeiro, M.G.S. Ribeiro, P.F. Keane, et al., Acid resistance of metakaolin-based, bamboo fiber geopolymer composites, Constr. Build. Mater., 302(2021), art. No. 124194. https://doi.org/10.1016/j.conbuildmat.2021.124194.

[33] R.B. Zhang, T. Liu, Y.M. Zhang, et al., Preparation of spent fluid catalytic cracking catalyst-metakaolin based geopolymer and its process optimization through response surface method, Constr. Build. Mater., 264(2020), art. No. 120727. https://doi.org/10.1016/j.conbuildmat.2020.120727.

[34] A.S. Srinivasa, K. Swaminathan, and S.C. Yaragal, Microstructural and optimization studies on novel one-part geopolymer pastes by Box-Behnken response surface design method, Case Stud. Constr. Mat., 18(2023), art. No. e01946. https://doi.org/10.1016/j.cscm.2023.e01946.

[35] V.C. Prabha, V. Revathi, and S.S. Reddy, Ambient cured high calcium fly ash geopolymer concrete with dolomite powder, Eur. J. Environ. Civ. Eng., 26(2022), No. 15, p.7857-7877. https://doi.org/10.1080/19648189.2021.2012262.

[36] Z.G. Shi, C.J. Shi, J. Zhang, et al., Alkali-silica reaction in waterglass-activated slag mortars incorporating fly ash and metakaolin, Cem. Concr. Res., 108(2018), p. 10-19. https://doi.org/10.1016/j.cemconres.2018.03.002.

[37] K.Y. Chen, D.Z. Wu, Z.L. Zhang, et al., Modeling and optimization of fly ash-slag-based geopolymer using response surface method and its application in soft soil stabilization, Constr. Build. Mater., 315(2022), art. No. 125723. https://doi.org/10.1016/j.conbuildmat.2021.125723.

[38] E.A. Dil, M. Ghaedi, G.R. Ghezelbash, et al., Highly efficient simultaneous biosorption of $Hg^{2+}$, $Pb^{2+}$ and $Cu^{2+}$ by Live yeast Yarrowia lipolytica 70562 following response surface methodology optimization: Kinetic and isotherm study, J. Ind. Eng. Chem., 48(2017), p. 162-172. https://doi.org/10.1016/j.jiec.2016.12.035.

[39] B.S. Mohammed, V.C. Khed, and M.F. Nuruddin, Rubbercrete mixture optimization using response surface methodology, J. Clean. Prod., 171(2018), p. 1605-1621. https://doi.org/10.1016/j.jclepro.2017.10.102.

[40] A. Özer, G. Gürbüz, A. Çalimli, et al., Biosorption of copper(II) ions on Enteromorpha prolifera: Application of response surface methodology (RSM), Chem. Eng. J., 146(2009), p. 377-387. https://doi.org/10.1016/j.cej.2008.06.041.

[41] Z.P. Li, D.G. Lu, and X.J. Gao, Optimization of mixture proportions by statistical experimental design using response surface method- A review, J. Build. Eng., 36(2021) 102101. https://doi.org/10.1016/j.jobe.2020.102101.

[42] Y. Zhang, Y. Wang, Z.G. Wu, et al., Optimal design of geopolymer grouting material for semi-flexible pavement based on response surface methodology, Constr.

Build. Mater., 306(2021), art. No. 124779. https://doi.org/10.1016/j.conbuildmat.2021.124779.

[43] C.L. Wong, K.H. Mo, U.J. Alengaram, et al., Mechanical strength and permeation properties of high calcium fly ash-based geopolymer containing recycled brick powder, J. Build. Eng., 32(2020), art. No. 101655. https://doi.org/10.1016/j.jobe.2020.101655.

[44] B.H. Zhu, R.E. Yu, J.Y. Shang, et al., The influence of NaOH concentration on the strength and microstructure of ceramic binders prepared from coal gangue through geopolymerization, Mater. Res. Express, 11(2024), No. 2, p. 025202. https://doi.org/10.1088/2053-1591/ad2a85.

[45] X.Y. Zhang, C.Q. Li, S.L. Zheng, et al., A review of the synthesis and application of zeolites from coal-based solid wastes, Int. J. Miner. Metall. Mater., 29(2022), No. 1, p. 1-21. https://doi.org/10.1007/s12613-021-2256-8.

[46] L. Long, Y.M. Zhao, G.J. Lv, et al., Improving stabilization/solidification of MSWI fly ash with coal gangue based geopolymer via increasing active calcium content, Sci. Total Environ., 854(2023), art. No. 158594. https://doi.org/10.1016/j.scitotenv.2022.158594.

[47] P.G. He, Q.K. Wang, S. Fu, et al., Hydrothermal transformation of geopolymers to bulk zeolite structures for efficient hazardous elements adsorption, Sci. Total Environ., 767(2021), art. No. 144973. https://doi.org/10.1016/j.scitotenv.2021.144973.

[48] Z.B. Öztürk, and A. İsmail İsa, Mechanical and microstructural characteristics of

geopolymer mortars at high temperatures produced with ceramic sanitaryware waste, Ceram. Int., 48(2022), No. 9, p. 12932-12944. https://doi.org/10.1016/j.ceramint.2022.01.166.

[49] S. Iftikhar, K. Rashid, E. Ul Haq, et al., Synthesis and characterization of sustainable geopolymer green clay bricks: An alternative to burnt clay brick, Constr. Build. Mater., 259(2020), art. No. 119659. https://doi.org/10.1016/j.conbuildmat.2020.119659.

[50] Z.J. Yang, D. Zhang, C.Y. Fang, et al., Hydration mechanisms of alkali-activated cementitious materials with ternary solid waste composition, Materials, 15(2022), No. 10, p. 3616. https://doi.org/10.3390/ma15103616.

[51] A. Kadhim, M. Sadique, R. Al-Mufti, et al., Long-term performance of novel high-calcium one-part alkali-activated cement developed from thermally activated lime kiln dust, J. Build. Eng., 32(2020), art. No. 101766. https://doi.org/10.1016/j.jobe.2020.101766.

[52] D.D. Burduhos Nergis, P. Vizureanu, A.V. Sandu, et al., XRD and TG-DTA study of new phosphate-based geopolymers with coal ash or metakaolin as aluminosilicate source and mine tailings addition, Materials, 15(2021), No. 1, p. 202. https://doi.org/10.3390/ma15010202.

[53] M. Akbelen, and N. Özbay, Influence of acid activation on hydrogen adsorption properties of analcime-rich tuff from Turkey, Turk. J. Chem., 46(2022), No. 5, p. 1565-1576. https://doi.org/10.55730/1300-0527.3461.

[54] P.J. Sánchez-Soto, E. Garzón, L. Pérez-Villarejo, et al., Mining wastes of an

albite deposit as raw materials for vitrified mullite ceramics, Minerals, 11(2021), No. 3, p. 232. https://doi.org/10.3390/min11030232.

[55] P. Jin, L. Li, Z. Li, et al., Using recycled brick powder in slag based geopolymer foam cured at ambient temperature: strength, thermal stability and microstructure, Constr. Build. Mater., 452(2024), art. No. 139008. https://doi.org/10.1016/j.conbuildmat.2024.139008.

[56] M.Y.J. Liu, U.J. Alengaram, M. Santhanam, et al., Microstructural investigations of palm oil fuel ash and fly ash based binders in lightweight aggregate foamed geopolymer concrete, Constr. Build. Mater., 120(2016), p. 112-122. https://doi.org/10.1016/j.conbuildmat.2016.05.076.

[57] E. Alvarez-Ayuso, X. Querol, F. Plana, et al., Environmental, physical and structural characterisation of geopolymer matrixes synthesised from coal (co-)combustion fly ashes, J. Hazard. Mater., 154(2008), No. 1-3, p. 175-183. https://doi.org/10.1016/j.jhazmat.2007.10.008.

[58] D.W. Zhang, K.F. Zhao, F.Z. Xie, et al., Effect of water-binding ability of amorphous gel on the rheology of geopolymer fresh pastes with the different NaOH content at the early age, Constr. Build. Mater., 261(2020), art. No. 120529. https://doi.org/10.1016/j.conbuildmat.2020.120529.